PCCP
Physical Chemistry Chemical Physics

Accepted Manuscript

This article can be cited before page numbers have been issued, to do this please use: T. Roccolano-Lindberg, L. M. Saleh Medina, M. A. Castro, A. Torres-Delgado, R. coneo-rodriguez, G. A. Planes, M. P. Longinotti and L. P. Méndez De Leo, *Phys. Chem. Chem. Phys.*, 2026, DOI: 10.1039/D6CP00137H.

View Article Online
DOI: 10.1039/D6CP00137H

ARTICLE

Tailored Mesoporous Carbons for High-Stability Supercapacitors with Optimized Ion Transport

Received 00th January 20xx,
Accepted 00th January 20xx

DOI: 10.1039/x0xx00000x

Tomás Roccolano-Lindberg,[a] Leila M. Saleh Medina,[a] María Ana Castro,[a] Angela Torres-Delgado,[b] Rusbel Coneo-Rodríguez,[b] Gabriel A. Planes,[b] María Paula Longinotti,*[a] Lucila P. Méndez De Leo*[a]

Mesoporous carbons with hierarchical porous architectures were synthesized via the carbonization of resorcinol-formaldehyde resins using mesoporous silica templates of varying pore sizes. The resulting carbon materials were extensively characterized to correlate their physicochemical properties with their electrochemical behavior as electrode materials for supercapacitors. Electrochemical performance was evaluated in both aqueous and organic electrolytes using cyclic voltammetry (CV), galvanostatic charge–discharge (GCD), and electrochemical impedance spectroscopy (EIS) in a three-electrode configuration. In addition, cycling stability using GDC was studied in two electrode cells, showing extremely high capacitance retention, especially in aqueous solution (99% after 20000 galvanostatic charge-discharge cycles). The results demonstrated that, although a high specific surface area contributes positively to charge storage, capacitance is strongly governed by the accessibility of electroactive sites, which in turn is influenced by pore size distribution, connectivity, and electrolyte ion dimensions. The synthesized mesoporous carbons show promise as electrode materials for supercapacitors, particularly for pseudocapacitive applications due to their relatively slow charge-discharge characteristics and high stability. This work underscores the critical role of mesostructure tuning in optimizing ion transport and charge storage dynamics, highlighting the potential of templated mesoporous carbons for high-performance electrochemical energy storage systems.

Introduction

The development of sustainable and renewable energy sources is a key challenge in our time, owing to the limitation of crude oil resources and its negative environmental impact, specially concerning the emission of CO_2 that causes global warming.[1–4] Renewable energy sources, on the other hand, are limited by their intermittency, making their efficient storage a very important issue of study, in order to guarantee effective, continuous, dependable and affordable energy supplies.[1,5] Electrochemical energy storage (EES) technologies, along with materials development, constitute essential elements to tackle the challenges to provide a stable supply of energy. Furthermore, depending on the design, EES can be environmentally friendly and versatile for the development of micro and macro devices, ranging from electronic skin, implantable medical devices, household and personal appliances, to electric vehicles.[6–8] It is of utmost importance to design systems that allow advances in new technologies with high efficiency, that involve the use of less expensive materials and that can withstand many charge-discharge cycles (high durability).[1,5] Batteries, fuel cells, and supercapacitors are some of the energy storage devices that rely on electrochemical processes; however, their charge storage mechanisms differ, resulting in different energy densities and power densities.[9–11] The basic differences between supercapacitors and batteries lie in their different charge storage mechanisms and the materials and structures of their electrodes. Typically, batteries and fuel cells are engineered for high energy density, storing substantial charge through Faradaic reactions in their electrodes or via reactants held in external reservoirs, respectively. In contrast, supercapacitors can provide high power density due to surface-based charge storage mechanisms. In addition, pseudocapacitors are a class of energy storage devices that combine the mechanisms of both batteries and supercapacitors. Acting as a bridge between the two, they offer high energy density while maintaining fast charge-discharge capabilities.[12–17] While electrochemical double-layer (EDL) capacitors store energy through charge separation at the Helmholtz layer of the electrode interface, pseudocapacitors derive their capacitance from Faradaic redox processes. Crucially, the performance of a high-quality pseudocapacitor relies on a robust capacitive foundation, ensuring that the Faradaic reactions are supported by an efficient double-layer structure.

The nature of double-layer capacitors energy storage devices is based on storage of electrical energy by charge separation at its

[a] Instituto de Química Física de los Materiales, Medio Ambiente y Energía (INQUIMAE – CONICET) y Departamento de Química Analítica, Inorgánica y Química Física, Facultad de Ciencias Exactas y Naturales, Universidad de Buenos Aires, Intendente Guiraldes 2160 – 1er piso, Buenos Aires, Argentina.
[b] Facultad de Ciencias Exactas, Fisicoquímicas y Naturales, Instituto de Investigaciones en Tecnologías Energéticas y Materiales Avanzados (IITEMA), Universidad Nacional de Río Cuarto-CONICET, Ruta Nac. 36, Km601, Río Cuarto, Córdoba, Argentina.

Supplementary Information available: [details of any supplementary information available should be included here]. See DOI: 10.1039/x0xx00000x

View Article Online
DOI: 10.1039/D6CP00137H

two electrodes with a developed voltage difference across the electrolyte. The capacitance of a double-layer supercapacitor depends on the surface area of the material used in the electrodes. [4,14,15,18,19]

Porous carbon materials are highly valued in nanotechnology due to their unique combination of properties, including large surface areas with good accessibility, high chemical and thermal stability, good electrical conductivity, intrinsic hydrophobicity, ease of surface chemistry modification, tunable nanostructure, morphology, and pore size, among others. These characteristics make them the obvious material of choice in supercapacitor electrodes.[16,17,20–23]

Theoretically, the higher the specific surface area, the higher the specific capacitance should be expected. However, practical situations are more complicated. No linear correlation can be found between surface area and capacitance.[3,8] Specific capacitance depends on the nature of the carbon, the surface area, and the pore structure of the electrode material. Likewise, ion size and electrolyte conductivity are closely related. Reducing the size of electrolyte ions can significantly improve their ability to diffuse into the electrode pores and adsorb on its surface, thereby improving the overall performance of the supercapacitor. As a result, pore size and ionic radius play a key role in improving charge storage performance, and it is important to understand how surface area, pore size, and carbon structure relate to a device's capacitance.[24–26]

Various synthesis methods have been explored to develop carbon materials featuring tailored morphologies and adjustable hierarchical pore size distributions.[27–29] Hierarchical carbon structures with tunable pore sizes can help address challenges such as long diffusion paths, slow ion transport, and pore clogging. Inorganic templates like porous silica or aluminosilicate offer well-defined porosity and structure. As such, using low-cost silica as a hard template—coupled with its relatively easy removal—enables the production of structured carbon materials of practical relevance without significantly increasing production costs.[30–34]

In this work, three mesoporous carbons were synthetized from structured resorcinol-formaldehyde resins using porous silica with different mesopore sizes as hard templates. The resulting materials were thoroughly characterized, and their performance as electrode materials in supercapacitors was studied, both in organic and aqueous media.

Experimental section

Materials

Resorcinol (99% Sigma-Aldrich), formaldehyde 37.7% w/w aqueous solution (Anhedra), sodium acetate trihydrate (p.a. Cicarelli), methanol and Glycerin (p.a. Biopack) were used as received. Silica mesoporous samples with particle size between 75-150 µm from Fuji Sylisia (CARIACT Qi, with i=3, 6 and 10, the mesoporous nominal pore diameter in nm), were used as received.

For electrochemical measurements, sulfuric acid (p.a. Cicarelli (95-98%)), acetonitrile (p.a. Sintorgan) and Bu_4NPF_6 (99% Fluka) were used. All aqueous solutions were prepared with 18 MOhm.cm Milli-Q deionized water.

Synthesis of mesoporous Carbons

Carbon mesoporous samples were synthesized using a procedure similar to that described by Fuentes Quezada et al.[33] by carbonization of a resorcinol-formaldehyde (RF) resin containing mesoporous silica (S) as hard template.

Briefly, mesoporous silica particles were dispersed in an aqueous solution containing resorcinol (R), a 37% w/w formaldehyde aqueous solution (F) and sodium acetate (C), used as catalyst. Glycerin (G) and methanol (MeOH) were then added to this solution to increase the viscosity, improve the dispersion of silica particles, decrease the surface tension of the medium and enhance the resin's permeability through the silica pores. The preparation of the resin precursor was performed using constant mass ratios R/F=1.15, R/C=8.30, R/H_2O=0.0215, R/G=0.29, and R/MeOH=0.5. The mass of silica CARIACT Q (S) was used for a constant ratio R/S=2. Polymerization of the resin was carried out at 120 °C under reflux for 155 minutes. The obtained product was then dried under vacuum at 60 °C for 24 hours. After pulverization, the product was carbonized in a tubular furnace in a nitrogen atmosphere with a heating ramp of 3 °C/min until reaching a temperature of 1000 °C. When this temperature value was attained, carbonization was carried out for 120 min. Silica was then removed from the carbon matrix by treatment with sodium hydroxide (NaOH, 3 M) at 60°C under reflux and constant stirring for 24 hours. Then, the carbon was filtered under vacuum and washed with deionized water to remove all traces of NaOH. Finally, the carbon was dried in a vacuum oven at 80°C for 24 hours.

Characterization Techniques

Scanning electron microscopy (SEM) measurements were performed with a SUPRATM 40 field emission SEM (Carl Zeiss SMT AG) working at an electron beam energy of 5 keV (CMA, FCEyN, UBA). The surface area of the materials was determined by measuring nitrogen sorption isotherms at liquid nitrogen temperature using a Micromeritics ASAP 2020 sortometer. The total surface and pore size distribution (PSD) were calculated using the Brunauer–Emmett–Teller (BET) model and a modified Barrett-Joyner-Halenda (BJH) model proposed by Villaroel-Rocha et al.[35] The t-plot method was used to obtain the microporous contribution, employing the thickness curve model by Broekhoff – de Boer. The measurements were done after degassing materials progressively at 50 mmHg for 1 h at room temperature, 1 mmHg for 1h at room temperature and finally unrestricted vacuum at 220°C for 24 h. XRD spectra were obtained using a Panalytical Empyrean powder diffractometer using Cu radiation, Kα1 = 0.154 nm, and equipped with a PIXcel3D area detector, in the range of 20 to 100 degrees, in theta/2 theta configuration, with a step of 0.026 degrees and a counting time of 50 seconds. The IR Transmission spectra for the mesoporous carbons in KBr pellets were performed on a Thermo Nicolet 8700 spectrometer using a MCT-A detector, 256 scans and a resolution of 4 cm^{-1}. Raman spectra were collected

View Article Online
DOI: 10.1039/D6CP00137H

in backscattering geometry with a LabRam HR Evolution Raman microspectrometer set at 1 cm^{-1} resolution and equipped with a Nd-Yaglaser line (532 nm). Beam power and acquisition times were optimized for each sample.

Electrode preparation

In order to test the mesoporous carbons as electrode materials, inks of all synthetized mesoporous carbon samples were prepared mixing around 75 mg of the corresponding mesoporous carbon (95 % w/w), around 4 mg of polyvinylidene fluoride (PVDF, Sigma Aldrich), used as binder, and 1.7 ml of N-methyl-2-pyrrolidone (Sigma Aldrich). 1 µL of the ink was then deposited on a previously polished glassy carbon electrode and dried with hot air.

Electrochemical characterization

Three electrode measurements

The electrochemical performance of the electrodes was evaluated using cyclic voltammetry (CV), galvanostatic charge–discharge (GCD), and electrochemical impedance spectroscopy (EIS) in a three-electrode testing system with a carbon counter electrode.

In aqueous media, a Ag/AgCl (3M KCl) reference electrode was used, while for organic (acetonitrile) media measurements, a non-aqueous $Ag/AgNO_3$ (0.1 M in acetonitrile) reference electrode was employed.

In CV experiments the potential window for measurements was determined by incrementally increasing the potential window and evaluating the coulombic efficiency of the resulting CVs, according to Mathis et al.[36] The exploratory CVs were performed at 0.01 $V.s^{-1}$ and the cutoff limit was chosen so that the coulombic efficiency dropped below 99%. Approximately, these values in aqueous solutions were around 0.0 V to 0.8 V, while in acetonitrile they were around –0.6 to 1.0 V. The scanning rate was varied from 0.01 $V.s^{-1}$ to 0.5 $V.s^{-1}$ in both media. The specific capacitance ($C_s(CV)$) was obtained according to:

$$C_s(CV) = \frac{\int_{V_i}^{V_f} i\, dV}{\nu\, \Delta V\, m}$$

Eq. 1

where the numerator represents the voltammetric charge, which is obtained by integrating the area of the reverse peak in the CV, ν is the scan rate used during the measurement, ΔV is the potential window, and m is the carbon mass in the active electrode.[4]

The GCD experiments were conducted in aqueous media within a potential range from 0.0 to 0.8 V, and from –0.6 to 1.0 V in acetonitrile. The current density was varied between 0.1 $A{\cdot}g^{-1}$ and 10 $A{\cdot}g^{-1}$. The specific capacitance, in this case, was calculated using:

$$C_s(GCD) = \frac{2\, i \int_{t_i}^{t_f} V\, dt}{(V_f^2 - V_i^2)}$$

Eq. 2

where i is the current density of the GCD experiment, the integral represents the area under the discharge curve of the GCD experiment, and V_f and V_i are the final and initial potentials of the charge-discharge process, as obtained from the CV experiments.

EIS experiments were carried out at the open circuit potential (OCP) under the application of a perturbation AC signal of 10 mV within a frequency range of 0.01 Hz–10000 Hz. Additionally, some experiments were carried out at potentials different from OCP.

The rate capability of supercapacitors is of great importance considering its practical application. In this context, EIS experiments can give significant information. Therefore, the real and imaginary contribution of the capacitance were calculated according to:[37]

$$C_s' = \frac{-Z''(\omega)}{\omega.|Z(\omega)|^2 m_{WE}} \qquad C_s'' = \frac{-Z'(\omega)}{\omega.|Z(\omega)|^2 m_{WE}}$$

Eq. 3

where C'_s and C''_s are the real and imaginary components of capacitance, respectively, m is the mass of carbon in the electrode, ω is the angular frequency, Z is the total complex impedance, Z'' is the imaginary part of the impedance, and Z' is the real part. In this analysis, the low frequency value of the real part of the capacitance corresponds to the capacitance of the cell that is measured during constant-current discharge, while the imaginary part of the capacitance is associated to an energy dissipation by an irreversible process that can lead to a hysteresis.[37] The dependence of C'_s and C''_s with frequency were analyzed and related to the dependence of the capacitance values obtained by CV measurements on the scan rate.[38–40]

Two electrode measurements

For two-electrode tests, a PTFE cell body with stainless steel current collectors was used for aqueous medium experiments. For organic medium, CR2032-type coin cells were used. Disks of expanded graphite (GRAFILIT® SF) were used as electrodes, loaded with an adequate quantity of mesoporous carbon ink (estimated from 3 electrode cell CVs) to obtain symmetric voltagrams, in order to maximize the capacitance retention.[8] Borosilicate glass microfiber filters (Whatman) embedded in Bu_4NPF_6 0.25M in acetonitrile solution or 1M H_2SO_4 aqueous solution were used as separators. In the case of coin cells, the assembly was performed in a glove box. Galvanostatic charge-discharge profiles were obtained with a Neware Battery Testing System BTS4000 5V-10 mA. The voltage window was adjusted to the value obtained from CV experiments, and the current density was chosen so that the charge-discharge time was between 1 and 1.5 minutes. At least 10000 cycles were tested.

The specific capacitance (C_s) in the two-electrode system was calculated according to[8,41]

$$C_s = \frac{I\Delta t}{m\Delta V}$$

Eq. 4

where I is the discharge current (A), Δt is the discharge time (s), m is the mass of carbon materials in the electrodes (g), and ΔV is the voltage change in the discharge process after ohmic drop (V). The energy density E (W.h.kg^{-1}) and power density P (W.kg^{-1}), based on the total mass of carbon materials in two electrodes, were calculated as follows:

$$E = \frac{1}{2}\frac{C_s}{4}V^2\frac{1}{3.6}$$
$$P = \frac{E}{t}$$

Eq. 5

where V is the cell voltage after ohmic drop (V) and t is the discharge time (h).

Results and Discussion

Physicochemical characterization of the mesoporous materials

Figure 1 shows the SEM micrographs of the three mesoporous samples synthesized in this work (panels a, b and c: CQ3, CQ6 and CQ10, respectively). Mesoporous carbons are called CQi where i is the pore size of the silica template. Micrographs show that all samples have randomly distributed pores with a porosity that increases when going from CQ3 to CQ10. Figure 1 (d) shows the XRD spectra of CQ3, CQ6 and CQ10 samples. All samples show a broad peak at around 2θ~23º that can be attributed to the (002) diffraction peak of carbon, showing a well-developed carbon stacking structure. Similar peaks, showing the formation of hard carbon, were also observed in other cases. The pattern of the peaks is typical of non-graphitic carbon materials with a highly disordered nano-crystalline structure, which is a proof of the presence of a hard carbon.[43,44] The appearance of broad peaks ensures the amorphous nature of these carbon materials. The d_{002} values were calculated using Bragg's equation ($n\lambda = 2\,d\,sin\vartheta$, where $n = 1$, λ is the wavelength, 0.154 nm).[45] The peaks appear at 2θ~23.02, 23.14 and 22.94 for CQ3, CQ6 and CQ10 respectively, indicating a mean interlayer distance (d_{002}) around 0.386 nm for all three samples. This value is higher than that of the well-ordered graphite (0.335 nm),[46,47] and can attributed to the presence of residual oxygen and hydrogen, probably derived from the precursor resin. This indicates that even though the carbonization was carried out in N_2(g), the resulting material has been partially oxidized during (or after) the synthetic process. This finding is supported by the IR spectra of the materials (Figure 1 (e)).

The IR spectra show a broad absorption peak at ~3400 cm^{-1}, attributed to O-H stretching, a peak at ~1630 cm^{-1}, ascribed to O-H and aromatic C=C bending, and a peak at ~1100 cm^{-1}, ascribed to -C-O- stretching. Surprisingly, no peak at ~1700 cm^{-1}, attributable to C=O stretching, was observed. These results indicate that the obtained materials are mainly graphene type with some superficial and residual oxidation. Raman spectra of the three mesoporous carbons exhibit the characteristic D and G bands of disordered carbon materials, centered at approximately 1340 and 1593 cm^{-1}, respectively. The I_D/I_G ratio is essentially the same for CQ3, CQ6 and CQ10 (1.09–1.10), indicating that the three carbons possess a very similar degree of structural disorder.[49,50] In all cases, only weak and broad signals are observed in the 2D region, without a defined maximum, supporting the poorly graphitized nature of the materials. The bandwidths of the D and G bands are also qualitatively very similar for the three samples. The RAMAN spectra are shown in figure S1 in Supplementary Information.

View Article Online DOI: 10.1039/D6CP00137H

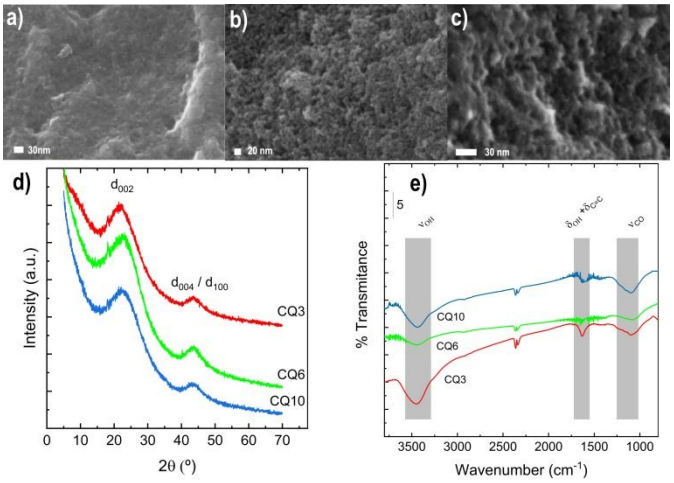

Figure 1: Scanning electron microscopy (SEM) images of the mesoporous carbon samples: (a) CQ3, (b) CQ6, and (c) CQ10. (d) Powder X-ray diffraction patterns, and (e) IR-spectra of the carbon samples.

XRD spectra (Figure 1(d)) also show that the 002 reflection peak is broad for all three samples, suggesting that they are very poorly ordered along the stacking direction. In addition, all samples show a broad but distinguishable peak at 2θ~44°, corresponding to 004 planes and/or 100 planes. The mean size of the ordered (crystalline) domains size L_c was estimated using the Scherrer equation:

$$Lc = \frac{A\,\lambda}{B\,cos\theta}$$

Eq. 6

where A is the shape factor (0.90, for amorphous carbon), λ the X-ray wavelength; θ the Bragg angle; and B is the full width at the half maximum of the peak in radians.[51] In all cases the mean size of the crystalline domains calculated was around 0.85 nm.

In order to further characterize the textural features of the carbon materials, N_2 adsorption and desorption isotherms were analyzed. Figure 2 (a) shows the obtained results, where it can be observed that isotherms are of type IV with hysteresis loops type II (H2), according to the classification given by IUPAC. The characteristic feature of H2 is that the hysteresis is wide, and

View Article Online
DOI: 10.1039/D6CP00137H

the adsorption branch is not parallel to the desorption branch. Like type I hysteresis (H1), H2 is characteristic of solids formed by particles crossed by almost cylindrical channels or made up of agglomerates or aggregates of spheroidal particles. Hysteresis loops of type II (H2) are characteristic of more complex pore structure in which network effects are important. For pore size analysis, VBS method[35] was employed on the adsorption branch. The adsorption branch is preferred when the closure of the hysteresis loop takes place around p/p_0 =0.42. The desorption branch in these conditions may be dominated by cavitation rather than by equilibrium evaporation from the pores. Cavitation leads to the sudden rupture of the condensed liquid phase inside the pores, which does not correspond to the true pore size.[52] The standard isotherm of non-porous carbon used to calculate statistical thickness was Cabot BP280.

Table 1 summarizes the results obtained for the textural properties of all samples. It can be observed that the mean pore diameters are 3.5, 4.0 and 3.4 nm for CQ3, CQ6, and CQ10 respectively, which indicates that, within the width of the PSD, all materials have similar pore diameters. These results indicate that, although the silica templates used to generate the different mesoporous carbons have different pore diameters, this does not influence the PSD of the carbon samples. This may be explained considering that all the silica templates are formed by agglomerates of silica particles of equal size, being the PSD of these materials determined by the interstices formed among the particles. Thus, the PSD of the carbon samples is determined by the size of the silica particles (equal for all Cariact Q samples), while the pores on the silica surface seem not to influence the PSD of the carbon material obtained. This kind of behavior has also been observed previously by Kruk et al.[52] in mesoporous carbons obtained by carbonization of sucrose using silica templates of different pore sizes. Small variations in PSD of the carbon samples can be given by contractions or expansions in the carbon matrix during the removal of the silica templates. The PSD obtained for all samples is similar to the smaller PSD peak obtained for samples synthesized by Quezada et al.[34] by the carbonization of a RF resine where they used Sipernat 50 as a HT and diallyldimethylammonium chloride (pDADMAC) as a soft template. However, in the work performed by these authors, a PSD centered around 9 nm was observed when only the HT was used as a pore structuring agent.

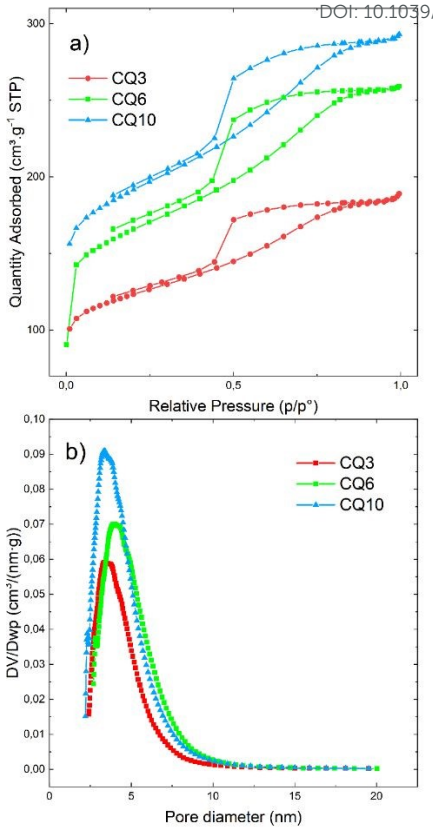

Figure 2: (a) N_2 adsorption and desorption isotherms measured at -196 °C, and (b) pore size distribution (PSD) determined from the BJH model (adsorption branch) for pristine carbon samples in the mesoporous region.

Table 1 also shows that the BET surface area, as well as the micro and mesopore volume increase from CQ3 to CQ10 (i.e. increasing the silica pore size), while the micropore percentage is approximately constant for all samples. This can be related to the fact that, as the pore size of the silica templates increases, the RF mixture is able to adhere to the silica templates in a better way, resulting in carbon samples with larger BET surface area and pore volume. Thus, in this study samples of similar pore diameters were obtained, with specific surface areas varying by up to 50 %.

Carbon samples obtained by Fuentes Quezada et al.,[33] by carbonization of a RF resine where only Sipernat 50 was used as HT have also a micropore volume content between 18 and 32% depending on the silica content.

Table 1: Textural features of the carbon samples synthesized in this work: pore diameter (d), BET surface area (SBET), micropore volume (V_{micro}), mesopore volume (V_{meso}), total volume (V_{total}) and fraction of the micropore volume (% V_{micr}).

	d (nm)	*SBET* ($m^2.g^{-1}$)	V_{micro} ($cm^3.g^{-1}$)	V_{meso} ($cm^3.g^{-1}$)	V_{total} ($cm^3.g^{-1}$)	% V_{micr}
CQ3	3.5	457	0.11	0.17	0.29	40
CQ6	4.0	606	0.14	0.26	0.40	35
CQ10	3.4	707	0.17	0.28	0.45	38

View Article Online
DOI: 10.1039/D5CP00137H

Electrochemical behavior characterization in a three electrode cell

Glassy carbon electrodes were modified as described before, and its electrochemical performance was evaluated using cyclic voltammetry (CV), galvanostatic charge–discharge (GCD), and electrochemical impedance spectroscopy (EIS) in a three-electrode testing system.

Behavior in acetonitrile:

Figure 3 shows the electrochemical behavior of the mesoporous carbon materials in 0.1M Bu_4NPF_6 in acetonitrile (Sintorgan). Panel (a) shows the cyclic voltammetries (CV) measured for all samples at a scan rate of 10 mV.s^{-1}, with the y-axis, expressed as specific capacitance, calculated according to $C_s=I/(mv)$ (*I:* current, *m*: mass of carbon in the electrode, *v:* scan rate). The CVs of all carbons exhibit a quasi-rectangular shape, indicating that materials behave as electrochemical double layer capacitors, where the ion transfer kinetic process is not limited,[21] with a contribution attributed to the resistivity of the material.[37] Panel (d) shows the CV (current density vs applied potential) measured for CQ6 at different scan rates while the CVs for CQ3 and CQ10 are shown in Figure S2 in the Supplementary Information.

The galvanostatic charge-discharge (GCD) curves in organic medium are shown in Figure 3 (b) for the three carbon samples at 0.125 A.g^{-1}. Figure 3 (e) shows the charge-discharge curves for CQ6 measured at different current densities; the charge-discharge curves for CQ3 and CQ10 are shown in Figure S2 in the Supplementary Information. The obtained profiles exhibit a quasi-triangular shape with (almost linear) charge and discharge curves characteristic of an ideal supercapacitor. The C_s calculated from Eq. 2 using the GCD data can be found in Table 2.The C_s values calculated through GCD data at a current density of 0.125 A.g^{-1} are close to the values determined by CV experiments at 10 mV.s^{-1}, and higher than those measured at 250 mV.s^{-1}, implying that the process of charge accumulation on the surface is somehow slow, and can advance to a considerable extent (though not necessary be completed) only if low scan rates, or low current densities are applied.

To further study the fundamental behavior of carbon samples, electrochemical impedance spectroscopy (EIS) was used. Nyquist plots of the three carbon materials are shown in Figure 3(c), where the equivalent circuit that fits properly the experimental data is added as an inset (values obtained for the elements of the equivalent circuit proposed are informed in the Supplementary Information, Table S1). Figure 3(f) shows the dependence of the imaginary component of the capacitance with frequency (calculated according to Eq. *3*). The maximum in the imaginary capacitance value defines the relaxation time, according to:

$$\tau_0 = \frac{1}{f_0}$$

Eq. 7

The relaxation time is characteristic of the system and also corresponds to the inverse of the frequency at which the real capacitance reaches half the maximum value of the real capacitance obtained at low frequency. At high frequency, the system behaves like a pure resistance, and the capacitance tends to 0 since the ions can only access the outer part of the carbon grains without entering the porous structure. On the other hand, at very low frequency, the capacitance reaches a maximum since the ions can access all the surface area of the pores. Between this two frequency boundaries, a transition region is observed where the capacitance varies linearly with frequency.[37,38,53,54] The time constant defines the frontier between the resistive and the capacitive behavior and can be useful to characterize the supercapacitor from an electrical point of view.[38] Table 2 shows the calculated relaxation times for the three carbons in acetonitrile. It can be observed that τ_0 (CQ6) > τ_0 (CQ3) > τ_0 (CQ10) and that all three times are greater than 10 s. These large relaxation times seem to be determined by the diffusion into the micropores.[55] Figure 4(a) shows the real contribution to the capacitance, C'_s, vs log frequency. It is clear that none of the samples reaches the expected plateau at low frequencies, showing a slow penetration of the electrolytes into the porous structure of the carbons. According to Segalini et al.,[53] there is a relationship between the micropore size and the frequency at which the transition from high to low frequency behavior happens. They showed that for their carbons, with monodisperse pores below 1 nm size, the transition from the low to high frequency behavior occurs at higher frequencies (lower relaxation times) when increasing the pore size. They consider that this behavior is related to the diffusion within the pores: bigger pores have higher diffusion constants and consequently the penetration within the pores is faster. Figure 4 (a) shows that, in the carbon samples synthesized in this work, the slope of the linear dependence of C_s vs frequency is not the same for all three samples, differently to what was observed in the samples of other authors.[53,54] Thus, our experiments cannot be interpreted within the context of the penetration rate related only to pore size, and might be explained considering that, according to N_2 adsorption experiments, while the mesopore size and the ratio between micro and meso pores is similar for all samples, the pore structure of the carbons is complex, leading to important network effects that may influence the electrolyte penetration into the pores. This behavior can also explain the crossover in the curves that describe the dependence of C_s vs scan rate determined from CVs experiments, presented in Figure 4 (b), that shows the C_s values determined for the different carbon samples studied as a function of scan rate in the CV experiment. C_s values for the three samples studied at 10 and 250 mV.s^{-1} scan rates are informed in Table 2. As expected, it can be noted that C_s decreases with the scan rate for all samples. This trend was also reported by Borchardt et al.[54], for tetraethylamonium tetrafluoroborate in acetonitrile solutions confined in carbons with different pore sizes. This tendency can be explained considering that at low scan rates the electrolytes have more time to diffuse into the porous samples and form the double layer in comparison to higher scan rates. Borchardt et al.[54] also

DOI: 10.1039/D6CP00137H

found that the decrease in capacitance with increasing scan rate is more important in samples presenting micropores than that observed in samples with only pores in the mesoporous range since diffusion within the smaller pores is more restricted. All our samples have similar pore size, with similar micropore contribution, which can explain the relatively small difference in the magnitude of the C_s values and its dependence on the scan rate. No relationship between C_s and the surface area of the samples is found.

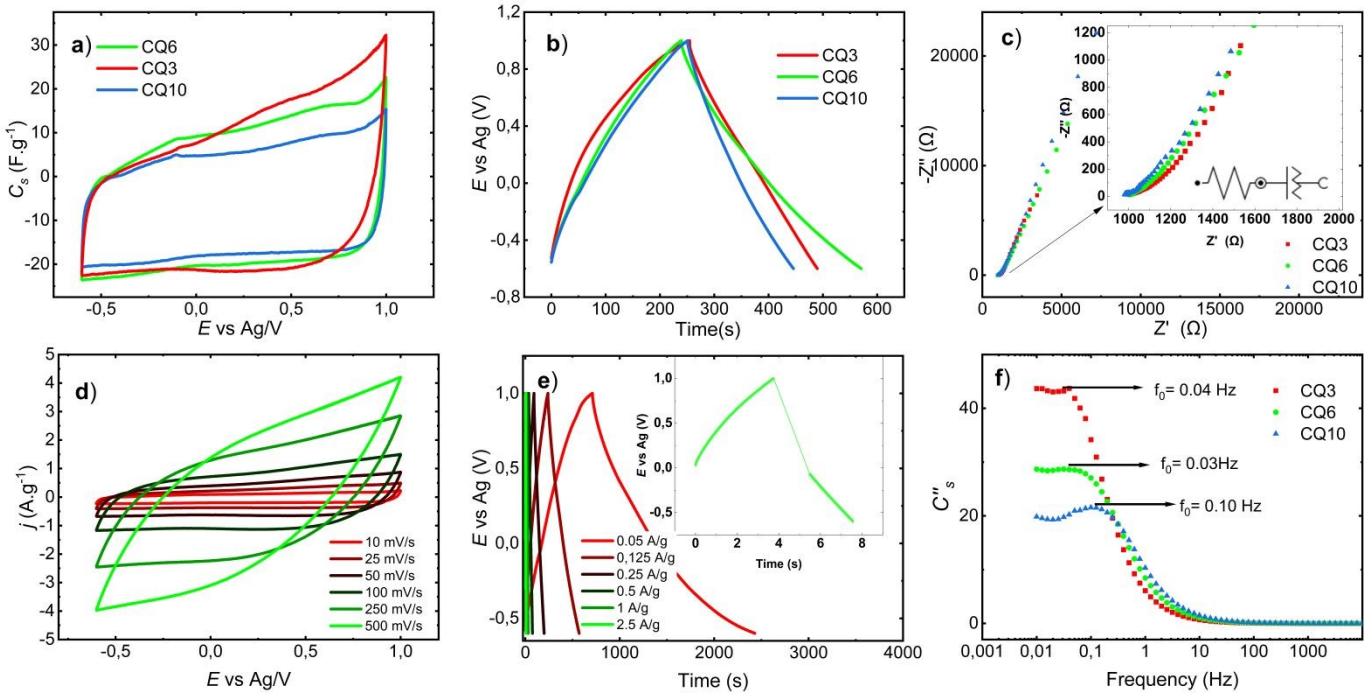

Figure 3: Electrochemical characterization of the behavior of the carbon samples synthesized in this work in 0.1M Bu_4NPF_6 in acetonitrile: (a) Cyclic Voltammetry (CV) measurements performed at 10 mV.s^{-1}, where C'_s was calculated according to $C_s=I/(mv)$ (I: current, m: mass of carbon in the electrode, v: scan rate) , (b) galvanostatic charge-discharge (GCD) curves at 0.125 A.g^{-1}, (c) Nyquist plots obtained from EIS experiments at OCP, (d) CV for CQ6 at different scan rates, (e) GCD curves for CQ6 at different density currents (inset: IR drop for GCD at 2.5 A.g^{-1}), and (f) $C''s$ vs frequency plots from EIS measurements.

View Article Online
DOI: 10.1039/D6CP00137H

ARTICLE

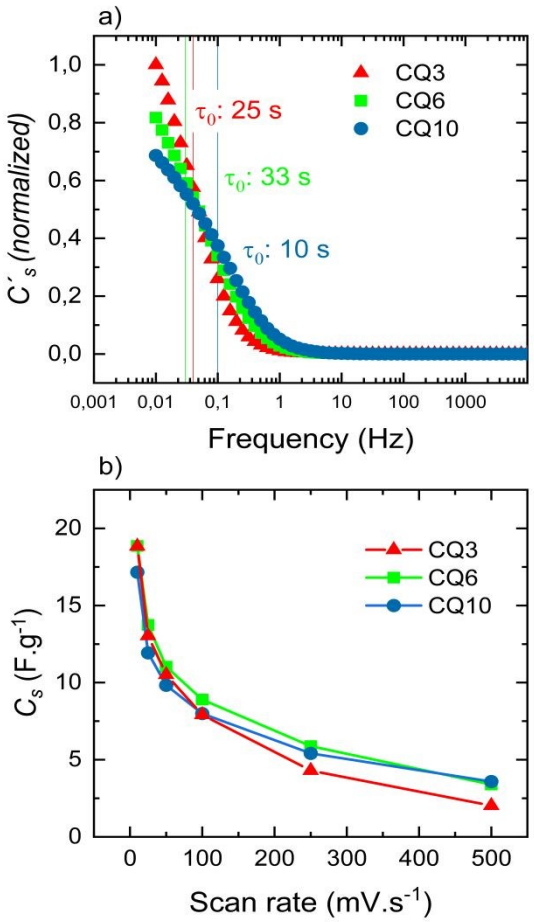

Figure 4: (a) Real contribution to the capacitance, *C´ (normalized)* vs log *f* and (b) C_s values obtained from CV experiments vs scan rate for the different carbon samples in 0.1M Bu_4NPF_6 in acetonitrile. Normalization in (a) respect the higher *C´* at the lowest frequency obtained (in this case for CQ3).

	C_s (F.g^{-1}) CV (10 mV.s^{-1})	C_s (F.g^{-1}) CV (250 mV.s^{-1})	C_s (F.g^{-1}) GDC (0.125 A.g^{-1})	Δ V (V)	τ_0 (s)
CQ3	18.8	4.3	16.7	1.6	25
CQ6	18.9	5.9	20.5	1.6	33
CQ10	17.2	5.4	12.6	1.6	10

Table 2: Specific capacitances in acetonitrile for all carbon samples, obtained from CV experiments at 10 and 250 mV.s^{-1} and from GCD measurements. Relaxation times (τ_0) determined from EIS measurements are also informed.

View Article Online
DOI: 10.1039/D6CP00137H

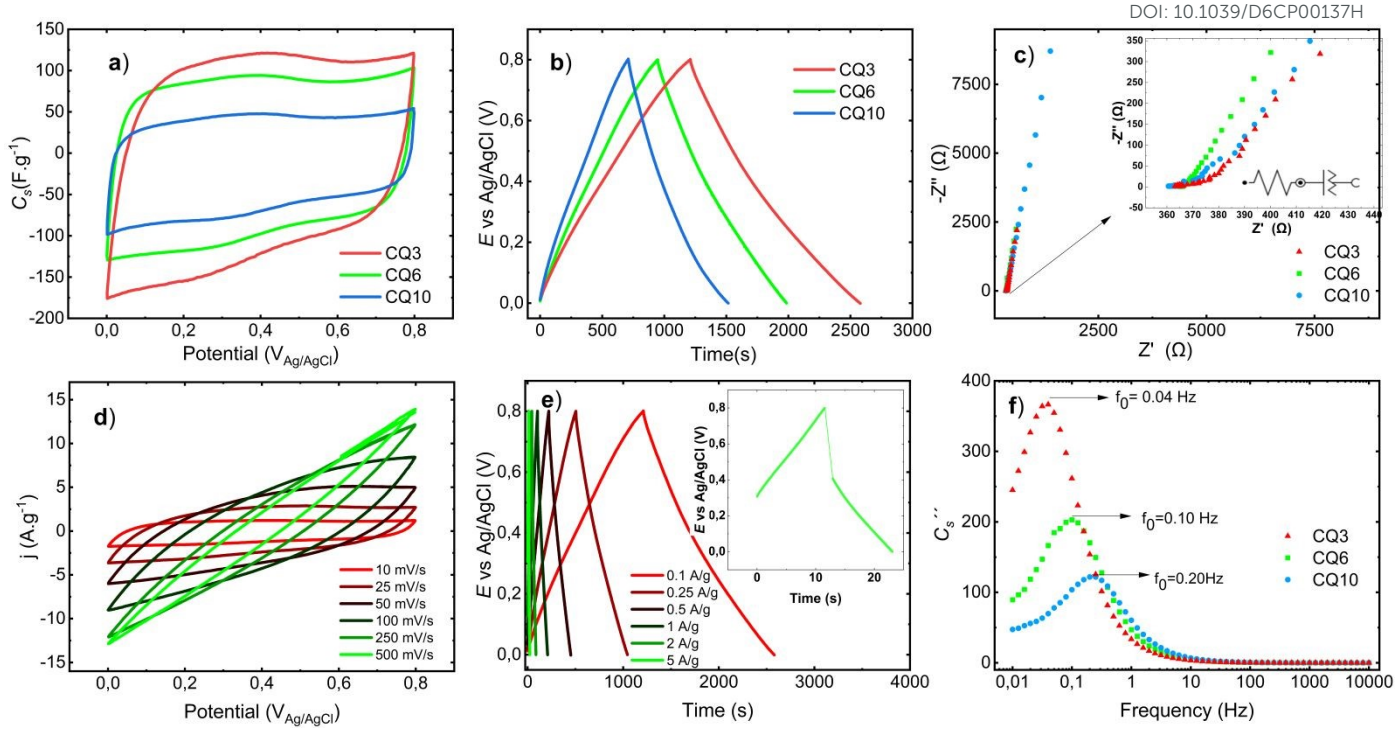

Figure 5: Electrochemical characterization of the behavior of the carbon samples synthesized in this work in 0.5 M H_2SO_4 aqueous solution: (a) Cyclic Voltametry (CV) measurements performed at 10 mV.s^{-1}, with the y axis expressed as C'_s (b) galvanostatic charge-discharge (GCD) curves at 0.1 A.g^{-1}. (c) Nyquist plots obtained from EIS experiments at OCP, (d) CV for CQ3 at different scan rates, (e) GCD curves for CQ3 at different density currents (inset: IR drop for GCD at 5 A.g^{-1}), (f), C''_s vs frequency plots from EIS measurements.

View Article Online
DOI: 10.1039/D6CP00137H

Behavior in aqueous solution:

Figure 5 shows the electrochemical behavior of the mesoporous carbon materials in aqueous media. Panel (a) shows the cyclic voltammetries (CV) measured for all samples at a scan rate of 10 mV.s^{-1}, with the y-axis expressed as specific capacitance. Panel (d) shows the CV (current density vs applied potential) measured for CQ3 at different scan rates while the CVs for CQ6 and CQ10 are shown in Figure S3 in Supplementary Information. As expected, in aqueous medium the capacitive behavior is similar to that observed in organic medium, with higher capacitance values and a smaller potential window.

Table 3: Specific capacitances in aqueous solution for the carbon samples synthesized in this work, obtained from CV experiments at 10 and 250 mV.s^{-1} and from GCD measurements. Relaxation times (τ_0), determined from EIS measurements are also informed.

	C_s (F.g^{-1}) CV (10 mV.s^{-1})	C_s (F.g^{-1}) CV (250 mV.s^{-1})	C_s (F.g^{-1}) GDC (0.1 A.g^{-1})	ΔV (V)	τ_0 (s)
CQ3	111.2	8.3	140.0	0.8	25
CQ6	89.0	14.8	109.2	0.8	10
CQ10	62.0	20.6	76.7	0.8	5

Table 3 shows the capacitance values obtained at 10 mV.s^{-1} and 250 mV.s^{-1} from CV curves. For high scan rates, 250 mV.s^{-1}, the calculated C_s varies with the surface area, that is, C_s decreases with decreasing surface area (C_s of CQ3<CQ6<CQ10). This tendency is not observed in 0.1 M Bu_4NPF_6 in acetonitrile, probably because the bulky ions present do not penetrate into the pores, as the smaller ions do in aqueous medium. For low scan rate values (i.e. 10 mV.s^{-1}), CQ3 shows higher capacitance than CQ6 and CQ10. This tendency cannot be explained considering the BET surface area.

Instead, the contribution of the broad peak that appears in the CVs around 0.35 V (vs. Ag/AgCl) (see Figure 5 a and d) has to be considered. This band can be attributed to the oxidation/reduction of quinone functional groups that appear to be present on the carbon surfaces. This band seems to be more pronounced on CQ3. This is in accordance with the IR spectra of the samples, that show a pronounced peak at ~1630 cm^{-1}, ascribed to OH and C=C functional moieties. This electrochemical process contributes to the capacitance of the material via pseudocapacitance and involves protons. The presence of this kind of surface functionality has also been observed and reported by other authors.[8,57] Thus, at low scan rates, the measured capacitance is predominantly governed by Faradaic processes arising from the redox activity of surface functional groups, which are more prominent in CQ3. As the scan rate increases, the influence of these kinetically limited Faradaic contributions diminishes relative to the electric double-layer capacitance, due to the differing rate dependencies of these mechanisms.

The galvanostatic charge-discharge (GCD) curves in aqueous medium are shown in Figure 5 (b). The profiles exhibit a quasi-triangular shape with (almost linear) charge and discharge curves, characteristic of an ideal supercapacitor,[37] as also observed in organic media. Figure 5 (e) shows the GCD curves measured for CQ3 at different applied currents, while the GCD curves corresponding to CQ6 and CQ10 are shown in Figure S3, Supplementary Information. The ohmic drop corresponding to GCD at 5 A.g^{-1} is shown in the inset. The C_s values, calculated using Eq. 2, are informed in Table 3. The variation of C_s with the carbon sample follows the same trend in GCD experiments as that observed at slow scan rates in CV experiments. However, C_s values calculated through GCD experiments are slightly higher than those calculated by CV in all cases, probably because the current density value chosen for the GCD experiments (0.1 A.g^{-1}) implied a slower process of charging of the capacitor than the lower scan rate used in the CV experiments (10 mV.s^{-1}).

The values of specific capacitance obtained for the samples is similar to that informed for other micro and/or mesoporous carbons of high area and much higher than that of carbons of lower surface area (such as Vulcan).[58–60]

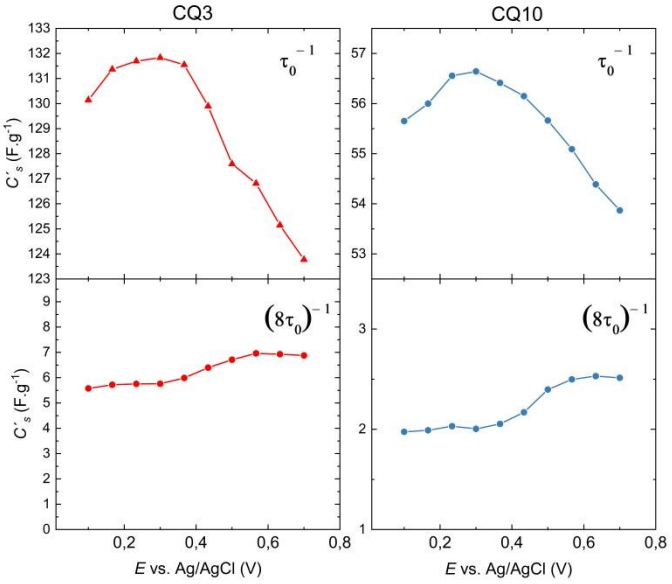

Figure 6: C´$_s$ values measured for CQ10 (blue) and CQ3 (red) as a function of applied potential by EIS experiments at different frequencies in 0.5 M H_2SO_4 aqueous solution

To further study the fundamental behavior of carbon samples in aqueous solutions, electrochemical impedance spectroscopy (EIS) was used. Nyquist plots of the three carbon materials are shown in Figure 5 (c). Figure (f) shows the dependence of the imaginary component of the capacitance with frequency. Table 3 shows the relaxation times obtained in aqueous medium. It can be observed that τ_0 for CQ3 is bigger than τ_0 for CQ6 and CQ10. This observation can be explained considering the faradaic process that contributes to the pseudocapacitive

View Article Online
DOI: 10.1039/D6CP00137H

behavior in CQ3, which is slow and retards the relaxation process in the carbon samples.

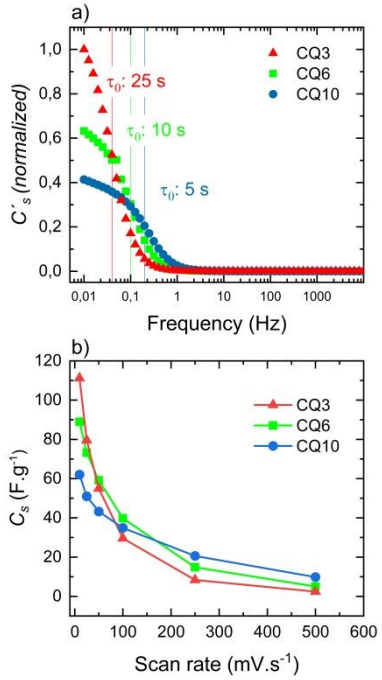

Figure 7: (a) Real contribution to the capacitance, C'_s, vs log f and (b) C_s values obtained from CV experiments vs scan rate for the different carbon samples in 0.5 M H_2SO_4 aqueous solution. Normalization in (a) respect the higher C' at the lowest frequency obtained (in this case for CQ3).

EIS additional experiments were carried out at potentials different from OCP, in order to separate the pseudacapacitive (faradaic) contribution to the measured capacitance from the exclusively supercapacitance (non-faradaic) contribution.[58] It can be expected that the faradaic contribution to capacitance (i.e., oxidation and reduction of the surface functional groups) will only occur if the applied potential is close to the potential of the redox couple on the surface, i.e. OCP. Figure 6 shows the variation of C'_s with the applied potential at fixed frequency values for CQ3 and CQ10 carbons. Two frequencies are shown for each carbonous material, corresponding to high frequency $(8\ \tau_0)^{-1}$ and low frequency (τ_0^{-1}). At high frequency, C'_s does not show a dependence on potential, while at low frequency, C'_s shows a maximum around 0.3 V vs Ag/AgCl. This can be explained considering that at this potential, if enough time is given to the process of charging the surface, a faradaic process contributes to the capacitance that, as mentioned before, and observed by other authors,[58] could be related to the oxidation/reduction of quinone surface functional groups. The contribution of the faradaic process is both observed in CQ3 and CQ10 mesoporous carbons, at low frequencies (comparable to τ_0^{-1}), but the height of the peak observed for CQ3 (8.06 $F.g^{-1}$) is almost three times higher than the corresponding to CQ10 (2.78 $F.g^{-1}$).

Figure 7(a) shows the real part of the capacitance vs. frequency and (b) the calculated capacitance by CV vs. scan rate. Again, as for organic media experiments (see before), different slopes are observed in the dependence of C'_s vs. log f in Figure 7 (a), probably due to the complex structure of the synthetized materials, that influence the electrolyte penetration into the pores. Accordingly, crossovers are observed in the curves of C_s vs v calculated from CVs experiments, seen in Figure 7(b).

Comparison of the behavior in aqueous and organic solution:

As expected, specific capacitance in aqueous solution is higher than in organic solution, while the stability window is greater in acetonitrile (see Table 2 and Table 3). The ionic size of the electrolyte and capacitance values are closely related.[57] The size of the ions and the that of the pores, as well as how the pores are interconnected, can greatly affect capacitance, especially under high current density values used in typical supercapacitors. Organic media tend to have lower ionic conductivity, and lower dielectric constants. Additionally, the larger ionic size of organic electrolytes makes it challenging for ions to diffuse into the pores. By reducing the size of the electrolyte ions, their ability to diffuse into the electrode's pores and adsorb onto its surface can be significantly improved. In this work, the size of the ions used in aqueous solutions (H^+ and SO_4^{2-}) is smaller than that of the ions used in acetonitrile (Bu_4N^+ and PF_6^-). In fact, among aqueous electrolytes, H_2SO_4 is widely used due to its high ionic conductivity at room temperature, that allows easy ion transport to the electrode surface, which results in great specific capacitance and low equivalent series resistance (ESR), leading to high energy and power density.[3,25] Figure 4 (a) and Figure 7 (a) show the specific real part of capacitance vs. frequency for acetonitrile and aqueous media, respectively. Comparing the shapes of the curves, it can be observed that while in aqueous media C'_s reaches a plateau at low frequencies, in acetonitrile this plateau is not observed at the accessible frequencies. This fact implies that in acetonitrile, the process of forming the double layer is slower than in aqueous media, probably due to higher ionic size, that makes it more difficult to diffuse into the complex porous structure of the material for the ions. This fact also affects the relaxation times, that are higher in acetonitrile, except for CQ3, where the faradaic process has a significative contribution to capacitance. A similar behavior was also observed in other systems where higher conductivity values result in smaller relaxation times.[38]

Table 4 summarizes the morphological and specific capacitances of the CQi carbons synthesized in this work in aqueous and organic media in comparison to data reported for different commercial samples.

Table 4: Morphological and electrochemical properties of carbon samples synthesized in this work compared with results for commercial carbons reported elsewhere.

View Article Online
DOI: 10.1039/D5CP01375H

Material	S_{BET} ($m^2.g^{-1}$)	V_{tot} ($cm^3.g^{-1}$)	V_{micro} (%)	Cs aqueous ($F.g^{-1}$)	Cs organic ($F.g^{-1}$)
Picactif	2410	1.63	40	111.0[a]	60.0[b]
CDC1	1656	0.85	74	115.1[a]	52.0[b]
Z carbon	1344	0.95	40	86.0[a]	48.0[b]
CDC2	1452	1.48	0	77.0[a]	56.0[b]
T carbon	1046	0.42	94	79.0[a]	20.1[b]
Vulcan	243	0,33	0	17.0[a]	14.0[b]
CQ3	457	0.29	40	111.2[c]	18.8[d]
CQ6	606	0.40	35	89.0[c]	18.9[d]
CQ10	707	0.45	38	62.0[c]	17.2[d]

[a] CV measurements at 20 mV/s in 0.5 M H_2SO_4.[58]
[b] CV measurements at 20 mV/s in 0.5M $TBAPF_6$ in acetonitrile.[58]
[c] CV measurements at 10 mV/s in 0.5 M H_2SO_4 (this work).
[d] CV measurements at 10 mV/s in 0.1M Bu_4NPF_6 in acetonitrile (this work).

The results demonstrate that among the carbon samples synthesized in this study, CQ3 exhibits the highest performance in aqueous electrolyte, attaining a specific capacitance of 111.2 $F{\cdot}g^{-1}$. Notably, this value is comparable to those obtained for the commercial benchmark Picactif (111.0 $F{\cdot}g^{-1}$) and reported in the literature for CDC1 (115.1 $F{\cdot}g^{-1}$)[58], despite CQ3 possessing a significantly lower specific surface area (457 $m^2{\cdot}g^{-1}$ vs. >1600 $m^2{\cdot}g^{-1}$). This discrepancy suggests highly efficient ion accessibility to the electroactive surface, likely enabled by an optimized pore size distribution and further enhanced by pseudocapacitive contributions from surface functional groups. Conversely, the electrochemical performance in organic medium (Bu_4NPF_6/ACN) shows a sharp decline to 17–19 $F{\cdot}g^{-1}$, values that align with the behavior of microporous carbons such as T carbon (20.1 $F{\cdot}g^{-1}$). This indicates that ion diffusion is severely restricted for bulkier organic ions. Consequently, while the CQ series proves competitive in aqueous systems, its limited performance in organic media underscores the critical necessity of tailoring the pore architecture to the specific dimensions of the electrolyte ions to sustain high power and energy densities.

3.3 Two-electrode analysis in organic and aqueous media.

Two-electrode configurations are fundamental for the accurate assessment of supercapacitor performance because they provide a representative evaluation of real-world device behavior by recording the absolute cell voltage between the positive and negative electrodes. This setup is the only reliable method to estimate the practical energy and power densities of the system, as well as the device response times, which are essential for comparing supercapacitors against established energy storage technologies.[4,61] Furthermore, evaluating cyclic stability is a critical performance index that defines the service life of the device by measuring the capacitance retention after thousands of cycles.[62] Thus, to further evaluate the electrochemical performance of the carbon materials, two-electrode tests were carried out in both aqueous and organic media. CQ6 was selected for the organic electrolyte and CQ3 for the aqueous one, based on their superior capacitance in the three-electrode configuration.

In the organic medium, coin cells were assembled as previously described. A total of 7.0 mg of CQ6 ink was deposited on the positive electrode and 5.0 mg on the negative electrode. The separators were soaked in 0.25 M Bu_4NPF_6 in acetonitrile, used as the electrolyte. A stable potential window of 2.7 V was achieved. Galvanostatic charge–discharge (GCD) curves were performed at a constant current of 2 mA, with each cycle lasting 58 s. The system was activated over 1000 cycles. The GCD curves exhibited good symmetry, indicating highly reversible charge–discharge behavior. The energy and power densities reached 3.78 $W.h.kg^{-1}$ and 522.7 $W.kg^{-1}$, respectively, with a coulombic efficiency of approximately 97%. After 9000 cycles, 85% of the initial capacitance was retained (initial and final charge-discharge curves are shown in Figure 8).

For the aqueous medium, a PTFE cell was used (see previous section). CQ3 ink was deposited on the positive (5.8 mg) and negative (5.0 mg) electrodes, using 1 M H_2SO_4 as the electrolyte. A potential window of 0.8 V was established. GCD tests were conducted at 4 mA, with each cycle lasting 82 s. The system required 500 activation cycles. The charge–discharge curves were symmetric, indicating good reversibility. The energy and power densities were 1.69 $W.h.kg^{-1}$ and 152.1 $W.kg^{-1}$, respectively, with a coulombic efficiency close to 99%. After 19500 cycles, 96% of the capacitance was preserved (see Figure 8 and Figure S4 in Supplementary Information). Additional parameters obtained before and after cycling are summarized in Table S2.

Overall, the materials synthesized in this work exhibit energy densities comparable to those reported for other mesoporous carbons, though with somewhat lower power densities.[63,64] However, their excellent capacitance retention highlights their outstanding cycling stability and long-term durability.

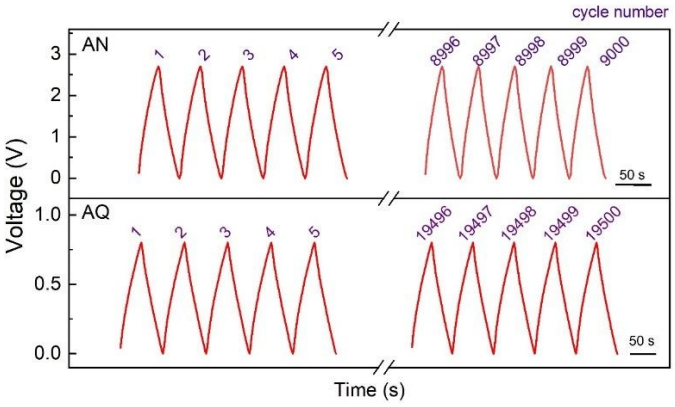

Figure 8: First and last five charge–discharge cycles for the two-electrode configuration. Top: in 0.1M Bu_4NPF_6 in acetonitrile. Bottom: in 0.5 M H_2SO_4 aqueous solution

Conclusions

View Article Online
DOI: 10.1039/D6CP00137H

Mesoporous carbons with complex hierarchical structures were synthetized and characterized. Three different samples were synthesized by carbonization of a resorcinol-formaldehyde resin containing mesoporous silica as hard template. Silica templates of particle size between 75-150 µm with pore nominal diameters between 3 and 10 nm were used. The carbon samples were characterized by SEM, XRD, IR, Raman and N_2 adsorption isotherms. The characterizations performed show that the materials obtained are non-graphitic carbons with a highly disordered nano-crystalline structure with mean interlayer distance (d_{002}) around 0.386 nm, indicating partial oxidation during the synthetic process, as supported by the appearance of typical OH and CO peaks in the IR spectra. N_2 adsorption and desorption isotherms analysis showed that all three samples have pore sizes around 3.7 nm, which may have been produced by the size of the silica particles used as hard templates, which are equal for all the silica samples. BET surface area, as well as the micro and mesopore volumes increase from CQ3 to CQ10, while the micropore percentage is approximately constant for all samples. This could be explained considering that the bigger the pore size of the silica templates, the better the resorcinol-formaldehyde mixture could adhere to the silica templates, resulting in carbon samples with a bigger BET surface area and pore volume. Moreover, the shape of the isotherms indicates that the pore structure is complex, with bottle-neck type pores, formed by particles crossed by almost cylindrical channels or made up of agglomerates or aggregates of spheroidal particles.

Exhaustive electrochemical characterization in 0.1 M Bu_4NPF_6 in acetonitrile and in 0.5 M H_2SO_4 aqueous solution was performed on inks prepared with the carbonous samples and deposited on glassy carbon electrodes in a three electrode cell. Capacitance was calculated from cyclic voltammetry, charge-discharge curves, and impedance spectroscopy analysis. In all cases, the typical behavior of an electrochemical double layer capacitor was obtained.

In organic medium, the difference in the C_s within the different samples is relatively small, and no relation between C_s *and the* surface area of the samples could be found. Electrochemical impedance measurements allowed to have an insight into the process of penetrating the mesoporous carbons by the ions. No relationship between the relaxation time and the maximum capacitance at low frequency was found, indicating a complex pore structure of the mesoporous carbons.

In aqueous media, while the capacitive behavior was dominant, a faradaic broad band appeared around 0.3 V for CQ3. This band can be attributed to the oxidation/reduction of quinone functional groups that appear to be present on the carbon surfaces. This faradaic/pseudocapacitive behavior was only observable in aqueous solution as it implies the consumption of protons and increases the specific capacitance of this sample. Likewise, since faradaic processes are slower than capacitive processes, this behavior was only observable at low scan rates in CV experiments. Once more, as for organic media experiments, different slopes were observed in all carbon samples in the dependence of C'_s *vs.* $\log f$ (Figure 7 (a)), probably due to the complex structure of the synthetized materials, that influence the electrolyte penetration into the pores.

The specific capacitance values obtained were reasonably high, both in aqueous and organic media, at slow scan rates (CV) and low currents (GCD curves). However, these values diminished rapidly as the scan rate/current increased. This behavior can be attributed to the tortuous pathways that ions must navigate to penetrate the pores, particularly in organic media where the ions are larger. This suggests that they are promising base-materials for functionalization with electroactive moieties, to be used in pseudocapacitors, where intrinsically slow faradaic processes are coupled to capacitance. The experiments carried out in two electrode systems showed that the materials are very stable, losing only 4% of capacitance after ~20000 cycles in aqueous medium, and around 15% in acetonitrile after 9000 cycles, probably due to solvent decomposition.[65] In summary, the synthesized materials exhibit energy densities, both in organic an aqueous media, comparable to other mesoporous carbons, with slightly lower power densities, yet their excellent capacitance retention demonstrates outstanding cycling stability and long-term durability.

Author contributions

Tomás Roccolano-Lindberg (Formal analysis: Equal; Investigation: Equal; Writing –original draft: Supporting; Writing – review & editing: Supporting)

Leila M. Saleh Medina (Formal analysis: Supporting; Investigation: Supporting; Methodology: Supporting; Writing – original draft: Supporting)

María Ana Castro (Formal analysis: Supporting; Investigation: Supporting; Methodology: Supporting; Writing – original draft: Supporting)

Angela Torres-Delgado (Investigation: Supporting)

Rusbel Coneo-Rodríguez (Writing – review & editing: Supporting)

Gabriel A. Planes (Investigation: Supporting; Writing – review & editing: Supporting)

María Paula Longinotti (Conceptualization: Lead; Investigation: Lead; Methodology: Lead; Supervision: Lead; Writing – original draft: Lead; Writing – review & editing:Lead)

Lucila Paula Méndez De Leo, Ph. D. (Conceptualization: Lead; Funding acquisition:Lead; Investigation: Lead; Methodology: Lead; Supervision: Lead; Writing – original draft: Lead; Writing – review & editing: Lead).

Conflicts of interest

There are no conflicts to declare.

View Article Online
DOI: 10.1039/D6CP00137H

Data availability

Data for this article are available at Google Drive at https://drive.google.com/drive/folders/16fvsG6A-T-I702BcdZFP8JU27US8ZbV2?usp=sharing.

Acknowledgements

This work was partially supported by Universidad de Buenos Aires, Argentina (20020220400015BA), Consejo Nacional de Investigaciones Científicas y Técnicas, Argentina (CONICET, PIP-11220200102008CO), Agencia Nacional de Promoción de la Investigación, el Desarrollo Tecnológico y la Innovación, Argentina (PICT-2020 SERIEA-01758) and Redes Federales de Alto Impacto, SICyT, Argentina (EX-2023-42139041- -APN-DDYGD#MCT). T.R.L. gratefully acknowledges a doctoral fellowship from CONICET, and L.M.S.M., M.A.C., R.C.R., G.A.P, M.P.L. and L.P.M.D.L. are research staff of CONICET.

Notes and references

1 Z. Yang, J. Zhang, M. C. W. Kintner-Meyer, X. Lu, D. Choi, J. P. Lemmon and J. Liu, Electrochemical Energy Storage for Green Grid, *Chemical Reviews*, 2011, **111**, 3577–3613.
2 S. P. S. Badwal, S. S. Giddey, C. Munnings, A. I. Bhatt and A. F. Hollenkamp, Emerging electrochemical energy conversion and storage technologies, *Frontiers in Chemistry*, 2014, **2**, 79.
3 A. Mendhe and H. S. Panda, A review on electrolytes for supercapacitor device, *Discover Materials*, 2023, **3**, 29.
4 A. Noori, M. F. El-Kady, M. S. Rahmanifar, R. B. Kaner and M. F. Mousavi, Towards establishing standard performance metrics for batteries, supercapacitors and beyond, *Chem. Soc. Rev.*, 2019, **48**, 1272–1341.
5 S. S. Siwal, Q. Zhang, N. Devi and V. K. Thakur, Carbon-Based Polymer Nanocomposite for High-Performance Energy Storage Applications, *Polymers*, 2020, **12**, 505.
6 A. Kumar Samantara and S. Ratha, *Electrochemical Energy Conversion and Storage Systems for Future Sustainability: Technological Advancements*, CRC Press, New York, 2021.
7 X. Zhang, X. Cheng and Q. Zhang, Nanostructured energy materials for electrochemical energy conversion and storage: A review, *Journal of Energy Chemistry*, 2016, **25**, 967–984.
8 Z. Chen, X. Wang, Z. Ding, Q. Wei, Z. Wang, X. Yang and J. Qiu, Biomass-based Hierarchical Porous Carbon for Supercapacitors: Effect of Aqueous and Organic Electrolytes on the Electrochemical Performance, *ChemSusChem*, 2019, **12**, 5099–5110.
9 T. M. Gür, Review of electrical energy storage technologies, materials and systems: challenges and prospects for large-scale grid storage, *Energy Environ. Sci.*, 2018, **11**, 2696–2767.
10 Q. Abbas, M. Mirzaeian, M. Hunt, P. Hall and R. Raza, Current State and Future Prospects for Electrochemical Energy Storage and Conversion Systems, *Energies*, 2020, **13**, 5847.
11 O. Haas and E. J. Cairns, Chapter 6. Electrochemical energy storage, *Annu. Rep. Prog. Chem., Sect. C: Phys. Chem.*, 1999, **95**, 163–198.
12 E. Murugan and M. Kaviya Sri, High energy density of Manganese Nickel oxide integrated imidazole functionalized multiwalled carbon nanotubes as supercapacitor electrodes, *Journal of Power Sources*, 2025, **653**, 237751.
13 X.-M. Cao, J.-Q. Chen, X.-R. Zhao, H. Ge, D. Liu, Q. Wu, Z.-J. Sun and Q. Zhang, Facile synthesis of bead-chain structured MWCNTs@CeO2 with oxygen vacancies-rich for promoting electrochemical energy storage, *Chemical Engineering Journal*, 2024, **479**, 147663.
14 B. E. Conway, *Electrochemical Supercapacitors Scientific Fundamentals and Technological Applications*, Springer, New York, NY, 2013.
15 A. Yu, V. Chabot and J. Zhang, *Electrochemical Supercapacitors for Energy Storage and Delivery*, CRC Press, Boca Raton, 2017.
16 S. Fleischmann, J. B. Mitchell, R. Wang, C. Zhan, D. Jiang, V. Presser and V. Augustyn, Pseudocapacitance: From Fundamental Understanding to High Power Energy Storage Materials, *Chem. Rev.*, 2020, **120**, 6738–6782.
17 J. N'Diaye, R. Bagchi, J. Y. Howe and K. Lian, Redox Active Organic-Carbon Composites for Capacitive Electrodes: A Review, *Sustainable Chemistry*, 2021, **2**, 407–440.
18 A. Pandolfo, V. Ruiz, S. Sivakkumar and J. Nerkar, in *Beguin, F & Frackowiak, E (Eds.) Supercapacitors: materials, systems, and applications*, Wiley-VCH, Germany, pp. 69–109.
19 B. K. Kim, S. Sy, A. Yu and J. Zhang, in *Handbook of Clean Energy Systems*, 2015, pp. 1–25.
20 E. Frackowiak and F. Béguin, Carbon materials for the electrochemical storage of energy in capacitors, *Carbon*, 2001, **39**, 937–950.
21 R. Y. N, K. Sharma and P. M. Shafi, An overview, methods of synthesis and modification of carbon-based electrodes for supercapacitor, *Journal of Energy Storage*, 2022, **55**, 105727.
22 A. B. Fuertes, G. Lota, T. A. Centeno and E. Frackowiak, Templated mesoporous carbons for supercapacitor application, *Electrochimica Acta*, 2005, **50**, 2799–2805.
23 A. Hryniewicka, G. Siemiaszko and M. E. Plonska-Brzezinska, Mesoporous Carbon Composites Containing Carbon Nanostructures: Recent Advances in Synthesis and Applications in Electrochemistry, *Materials*, DOI:10.3390/ma17246195.
24 F. Béguin, V. Presser, A. Balducci and E. Frackowiak, Carbons and Electrolytes for Advanced Supercapacitors, *Advanced Materials*, 2014, **26**, 2219–2251.
25 G. Song, C. Li, T. Wang, K. H. Lim, F. Hu, S. Cheng, E. Hondo, S. Liu and S. Kawi, Hierarchical Hollow Carbon Particles with Encapsulation of Carbon Nanotubes for High Performance Supercapacitors, *Small*, 2024, **20**, 2305517.
26 N. Velychkivska, A. Golunova, A. Panda, P. A. Shinde, R. Ma, K. Ariga, Y. Yamauchi, J. P. Hill, J. Labuta and L. K. Shrestha, Ultrahigh Surface Area Hierarchically Porous Carbon Materials from Polyacrylamide–Cellulose Hydrogel for High-Performance Supercapacitors, *ACS Appl. Energy Mater.*, 2024, **7**, 2906–2917.
27 N. D. Petkovich and A. Stein, Controlling macro- and mesostructures with hierarchical porosity through combined hard and soft templating, *Chem. Soc. Rev.*, 2013, **42**, 3721–3739.
28 A. Stein, Z. Wang and M. A. Fierke, Functionalization of Porous Carbon Materials with Designed Pore Architecture, *Advanced Materials*, 2009, **21**, 265–293.
29 C. Liang, Z. Li and S. Dai, Mesoporous Carbon Materials: Synthesis and Modification, *Angewandte Chemie International Edition*, 2008, **47**, 3696–3717.
30 R. Ryoo, S. H. Joo and S. Jun, Synthesis of Highly Ordered Carbon Molecular Sieves via Template-Mediated Structural Transformation, *J. Phys. Chem. B*, 1999, **103**, 7743–7746.
31 J. H. Knox, B. Kaur and G. R. Millward, Structure and performance of porous graphitic carbon in liquid chromatography, *Journal of Chromatography A*, 1986, **352**, 3–25.
32 K. P. Gierszal, T.-W. Kim, R. Ryoo and M. Jaroniec, Adsorption and Structural Properties of Ordered Mesoporous Carbons Synthesized by Using Various Carbon Precursors and Ordered Siliceous P6mm and Ia3d Mesostructures as Templates, *J. Phys. Chem. B*, 2005, **109**, 23263–23268.
33 E. Fuentes-Quezada, E. de la Llave, E. Halac, M. Jobbágy, F. A. Viva, M. M. Bruno and H. R. Corti, Bimodal mesoporous hard carbons from stabilized resorcinol-formaldehyde resin and silica template with enhanced adsorption capacity, *Chemical Engineering Journal*, 2019, **360**, 631–644.
34 E. Fuentes-Quezada, D. C. Martínez-Casillas, A. K. Cuentas Gallegos and E. De La Llave, Effect of Hierarchical Porosity on PMo12Adsorption and Capacitance in Hybrid Carbon-PMo12Electrodes for Supercapacitors, *Energy and Fuels*, 2022, **36**, 3987–3996.
35 J. Villarroel-Rocha, D. Barrera and K. Sapag, Introducing a self-consistent test and the corresponding modification in the Barrett, Joyner and

Halenda method for pore-size determination, *Microporous and Mesoporous Materials*, 2014, **200**, 68–78.
36 T. S. Mathis, N. Kurra, X. Wang, D. Pinto, P. Simon and Y. Gogotsi, Energy Storage Data Reporting in Perspective—Guidelines for Interpreting the Performance of Electrochemical Energy Storage Systems, *Advanced Energy Materials*, 2019, **9**, 1902007.
37 P. L. Taberna, P. Simon and J. F. Fauvarque, Electrochemical Characteristics and Impedance Spectroscopy Studies of Carbon-Carbon Supercapacitors, *Journal of The Electrochemical Society*, 2003, **150**, A292.
38 M. Itagaki, S. Suzuli, I. Shitanda and K. Watanabe, Electrochemical Impedance and Complex Capacitance to Interpret Electrochemical Capacitor, *Electrochemistry*, 2007, **75**, 649–655.
39 J. H. Jang and S. M. Oh, Complex Capacitance Analysis of Porous Carbon Electrodes for Electric Double-Layer Capacitors, *Journal of The Electrochemical Society*, 2004, **151**, A571.
40 S. Yoon, J. H. Jang, B. H. Ka and S. M. Oh, Complex capacitance analysis on rate capability of electric-double layer capacitor (EDLC) electrodes of different thickness, *Electrochimica Acta*, 2005, **50**, 2255–2262.
41 S. Roldán, D. Barreda, M. Granda, R. Menéndez, R. Santamaría and C. Blanco, An approach to classification and capacitance expressions in electrochemical capacitors technology, *Phys. Chem. Chem. Phys.*, 2015, **17**, 1084–1092.
42 T. Zheng, W. Xing and J. R. Dahn, Carbons prepared from coals for anodes of lithium-ion cells, *Carbon*, 1996, **34**, 1501–1507.
43 C. Lin and J. A. Ritter, Effect of synthesis pH on the structure of carbon xerogels, *Carbon*, 1997, **35**, 1271–1278.
44 N. Parveen, M. O. Ansari, S. A. Ansari and M. H. Cho, Simultaneous sulfur doping and exfoliation of graphene from graphite using an electrochemical method for supercapacitor electrode materials, *J. Mater. Chem. A*, 2016, **4**, 233–240.
45 C. Nethravathi and M. Rajamathi, Chemically modified graphene sheets produced by the solvothermal reduction of colloidal dispersions of graphite oxide, *Carbon*, 2008, **46**, 1994–1998.
46 S. Ghosh, R. Santhosh, S. Jeniffer, V. Raghavan, G. Jacob, K. Nanaji, P. Kollu, S. K. Jeong and A. N. Grace, Natural biomass derived hard carbon and activated carbons as electrochemical supercapacitor electrodes, *Scientific Reports*, 2019, **9**, 16315.
47 D. Ma, X. Li, Y. Guo and Y. Zeng, Study on IR Properties of Reduced Graphene Oxide, *IOP Conference Series: Earth and Environmental Science*, 2018, **108**, 022019.
48 V. H. Pham, T. V. Cuong, S. H. Hur, E. Oh, E. J. Kim, E. W. Shin and J. S. Chung, Chemical functionalization of graphene sheets by solvothermal reduction of a graphene oxide suspension in N-methyl-2-pyrrolidone, *J. Mater. Chem.*, 2011, **21**, 3371–3377.
49 A. C. Ferrari and J. Robertson, Interpretation of Raman spectra of disordered and amorphous carbon, *Phys. Rev. B*, 2000, **61**, 14095–14107.
50 A. C. Ferrari and J. Robertson, Raman spectroscopy of amorphous, nanostructured, diamond–like carbon, and nanodiamond, *Philosophical Transactions of the Royal Society A: Mathematical, Physical and Engineering Sciences*, 2004, **362**, 2477–2512.
51 Y. P. Wu, S. Fang, Y. Jiang and R. Holze, Effects of doped sulfur on electrochemical performance of carbon anode, *Journal of Power Sources*, 2002, **108**, 245–249.
52 M. Thommes, K. Kaneko, A. V. Neimark, J. P. Olivier, F. Rodriguez-Reinoso, J. Rouquerol and K. S. W. Sing, Physisorption of gases, with special reference to the evaluation of surface area and pore size distribution (IUPAC Technical Report), 2015, **87**, 1051–1069.
53 M. Kruk, M. Jaroniec, R. Ryoo and S. H. Joo, Characterization of Ordered Mesoporous Carbons Synthesized Using MCM-48 Silicas as Templates, *J. Phys. Chem. B*, 2000, **104**, 7960–7968.
54 J. Segalini, B. Daffos, P. L. Taberna, Y. Gogotsi and P. Simon, Qualitative Electrochemical Impedance Spectroscopy study of ion transport into sub-nanometer carbon pores in Electrochemical Double Layer Capacitor electrodes, *Electrochimica Acta*, 2010, **55**, 7489–7494.
55 L. Borchardt, D. Leistenschneider, J. Haase and M. Dvoyashkin, Revising the Concept of Pore Hierarchy for Ionic Transport in Carbon Materials for Supercapacitors, *Advanced Energy Materials*, 2018, **8**, 1800892.
56 D. Qu and H. Shi, Studies of activated carbons used in double-layer capacitors, *Journal of Power Sources*, 1998, **74**, 99–107.
57 M. G. Sullivan, B. Schnyder, M. Bärtsch, D. Alliata, C. Barbero, R. Imhof and R. Kötz, Electrochemically Modified Glassy Carbon for Capacitor Electrodes Characterization of Thick Anodic Layers by Cyclic Voltammetry, Differential Electrochemical Mass Spectrometry, Spectroscopic Ellipsometry, X-Ray Photoelectron Spectroscopy, FTIR, and AFM, *Journal of The Electrochemical Society*, 2000, **147**, 2636.
58 S. Vaquero, R. Díaz, M. Anderson, J. Palma and R. Marcilla, Insights into the influence of pore size distribution and surface functionalities in the behaviour of carbon supercapacitors, *Electrochimica Acta*, 2012, **86**, 241–247.
59 M. M. Bruno, N. G. Cotella and C. A. Barbero, Hierarchical Biobased Macroporous/Mesoporous Carbon: Fabrication, Characterization and Electrochemical/Ion Exchange Properties, *Materials*, 2023, **16**, 2101.
60 M. Nazhipkyzy, M. Yeleuov, S. T. Sultakhan, A. B. Maltay, A. A. Zhaparova, D. D. Assylkhanova and R. R. Nemkayeva, Electrochemical Performance of Chemically Activated Carbons from Sawdust as Supercapacitor Electrodes, *Nanomaterials*, DOI:10.3390/nano12193391.
61 J. Zhao, Y. Gao and A. F. Burke, Performance testing of supercapacitors: Important issues and uncertainties, *Journal of Power Sources*, 2017, **363**, 327–340.
62 Q. Wu, T. He, Y. Zhang, J. Zhang, Z. Wang, Y. Liu, L. Zhao, Y. Wu and F. Ran, Cyclic stability of supercapacitors: materials, energy storage mechanism, test methods, and device, *J. Mater. Chem. A*, 2021, **9**, 24094–24147.
63 X. Chen, R. Paul and L. Dai, Carbon-based supercapacitors for efficient energy storage, *National Science Review*, 2017, **4**, 453–489.
64 Q. Dou and H. S. Park, Perspective on High-Energy Carbon-Based Supercapacitors, *ENERGY & ENVIRONMENTAL MATERIALS*, 2020, **3**, 286–305.
65 E. Pameté, L. Köps, F. A. Kreth, S. Pohlmann, A. Varzi, T. Brousse, A. Balducci and V. Presser, The Many Deaths of Supercapacitors: Degradation, Aging, and Performance Fading, *Advanced Energy Materials*, 2023, **13**, 2301008.

Hard Templated Mesoporous Carbons for High-Energy-Density Supercapacitors

View Article Online
DOI: 10.1039/D6CP00137H

Tomás Roccolano-Lindberg,[a] Leila M. Saleh Medina, [a] Angela Torres-Delgado,[b] Rusbel Coneo-Rodríguez, [b] Gabriel A. Planes, [b] María Paula Longinotti,*[a] Lucila P. Méndez De Leo*[a]

[a]Instituto de Química Física de los Materiales, Medio Ambiente y Energía (INQUIMAE – CONICET) y Departamento de Química Analítica, Inorgánica y Química Física, Facultad de Ciencias Exactas y Naturales, Universidad de Buenos Aires, Intendente Guiraldes 2160 – 1er piso, Buenos Aires, Argentina.

[b]Facultad de Ciencias Exactas, Fisicoquímicas y Naturales, Instituto de Investigaciones en Tecnologías Energéticas y Materiales Avanzados (IITEMA), Universidad Nacional de Río Cuarto-CONICET, Ruta Nac. 36, Km601, Río Cuarto, Córdoba, Argentina.

Data availability

Data for this article are available at Google Drive at https://drive.google.com/drive/folders/16fvsG6A-T-I702BcdZFP8JU27US8ZbV2?usp=sharing.